


# Thermoresponsive fiber-based microwells capable of formation and retrieval of salivary gland stem cell spheroids for the regeneration of irradiation-damaged salivary glands

Hye Jin Hong<sup>1\*</sup>, Jae-Min Cho<sup>2\*</sup>, Yeo-Jun Yoon<sup>2</sup>,  
 Dojin Choi<sup>2</sup>, Soohyun Lee<sup>2</sup>, Hwajung Lee<sup>1</sup>, Sujeong Ahn<sup>1</sup>,  
 Won-Gun Koh<sup>1</sup> and Jae-Yol Lim<sup>2</sup> 

## Abstract

Three-dimensional spheroid culture enhances cell-to-cell interactions among stem cells and promotes the expression of stem cell properties; however, subsequent retrieval and delivery of these cells remain a challenge. We fabricated a thermoresponsive fiber-based microwell scaffold by combining electrospinning and hydrogel micropatterning. The resultant scaffold appeared to facilitate the formation of cellular spheroids of uniform size and enabled the expression of more stem cell-secreting growth factor genes (*EGF*, *IGF-1*, *FGF1*, *FGF2*, and *HGF*), pluripotent stem cell-related genes (*SOX2* and *NANOG*), and adult epithelial stem cell-related genes (*LGR4*, *LGR5*, and *LGR6*) than salivary gland stem cells in a monolayer culture (SGSC<sup>monolayer</sup>). The spheroids could be retrieved efficiently by decreasing temperature. SGSC-derived spheroid (SGSC<sup>spheroid</sup>) cells were then implanted into the submandibular glands of mice at 2 weeks after fractionated X-ray irradiation at a dose of 7.5 Gy/day. At 16 weeks post-irradiation, restoration of salivary function was detected only in SGSC<sup>spheroid</sup>-implanted mice. The production of submandibular acini specific mucin increased in SGSC<sup>spheroid</sup>-implanted mice, compared with PBS control. More MIST1<sup>+</sup> mature acinar cells were preserved in the SGSC<sup>spheroid</sup>-implanted group than in the PBS control group. Intriguingly, SGSC<sup>spheroid</sup>-implanted mice exhibited greater amelioration of tissue damage and preservation of KRT7<sup>+</sup> terminally differentiated luminal ductal cells than SGSC<sup>monolayer</sup>-implanted mice. The SGSC<sup>spheroid</sup>-implanted mice also showed less DNA damage and apoptotic cell death than the SGSC<sup>monolayer</sup>-implanted mice at 2 weeks post-implantation. Additionally, a significant increase in Ki67<sup>+</sup>AQP5<sup>+</sup> proliferative acinar cells was noted only in SGSC<sup>spheroid</sup>-implanted mice. Our results suggest that a thermoresponsive fiber-based scaffold could be of use to facilitate the production of function-enhanced SGSC<sup>spheroid</sup> cells and their subsequent retrieval and delivery to damaged salivary glands to alleviate radiation-induced apoptotic cell death and promote salivary gland regeneration.

## Keywords

Salivary glands, stem cell spheroid, thermoresponsive fiber, fiber-based microwell, spheroid retrieval

Date received: 1 December 2021; accepted: 19 February 2022

<sup>1</sup>Department of Chemical and Biomolecular Engineering, Yonsei University, Seoul, Republic of Korea

<sup>2</sup>Department of Otorhinolaryngology, Gangnam Severance Hospital, Yonsei University College of Medicine, Seoul, Republic of Korea

\*These authors contributed equally to this work as co-first authors.

## Corresponding authors:

Won-Gun Koh, Department of Chemical and Biomolecular Engineering, Yonsei University, 50 Yonsei-ro, Seodaemun-gu, Seoul 03722, Republic of Korea.  
 Email: [wongun@yonsei.ac.kr](mailto:wongun@yonsei.ac.kr)

Jae-Yol Lim, Department of Otorhinolaryngology, Gangnam Severance Hospital, Yonsei University College of Medicine, 211 Eonju-ro, Gangnam-gu, Seoul 06273, Republic of Korea.  
 Email: [jylimd@yuhs.ac](mailto:jylimd@yuhs.ac)



## Introduction

Cell therapy techniques using mesenchymal stem cells (MSCs) or tissue-resident stem cells have been developed for the prevention, repair, and restoration of salivary gland hypofunction.<sup>1</sup> However, the therapeutic potential of locally injected or systemically infused stem cells is limited by substantial cell death caused by anoikis or entrapment in non-target tissues, including those of the lungs and kidneys.<sup>2</sup> To improve survival and therapeutic efficacy, stem cells have been implanted *in vivo* using carrier scaffolds or primed to promote stem cell survival and the ability to differentiate or secrete therapeutic factors, including cytokines and growth factors, before implantation.<sup>3</sup> Among various stem cell engineering technologies, 3-dimensional (3D) culturing of stem cell spheroids has been suggested to increase engraftment efficiency and therapeutic efficacy in target tissues due to their relatively large volume, their reduced apoptosis levels, and their enhanced stem cell properties, which enable them to survive harsh environments in recipient tissues.<sup>4</sup> MSC spheroids derived from human bone marrow or adipose tissue have been found to exhibit enhanced secretion of anti-inflammatory, anti-apoptotic, and angiogenic cytokines or growth factors, enabling a higher therapeutic efficacy in various ischemic and injury models.<sup>5–8</sup> Notwithstanding, if stem cell spheroids are to be used as implantable therapeutics, several challenges related to spheroid size control, mass production, and degradation during their harvest and delivery into target tissues must be addressed.

Generally, *in vitro* cellular spheroids are produced using hanging drops, spinner flasks, and microwells.<sup>9,10</sup> Of these, microwells have become popular recently because they can produce many spheroids of uniform size. Microwells can be fabricated using various microfabrication techniques, which enable the formation of spheroids of desired sizes.<sup>11–13</sup> However, most microwell-based platforms are generated on plane substrates and do not completely mimic the native nanostructure of the extracellular matrix (ECM). Meanwhile, electrospun nano/microfibers are widely used as tissue engineering scaffolds because they can recapitulate aspects of native ECM for *in vitro* cell cultures.<sup>14–16</sup> Indeed, fibrous scaffold has been shown to promote spheroid formation of anchorage dependent cells with better efficiency than conventional methods.<sup>17</sup> Researchers have also reported that fibrous scaffolds enhance cell-cell interactions and stimulate spheroid formation in MSCs, resulting in enhanced cell proliferation and expression of stem cell markers, as well as maintenance of their stemness and multilineage differentiation potential.<sup>18</sup> The positive effects of electrospun fibers on the spheroid formation result from several advantages of the fibrous scaffolds, including biomimicking topographical and biochemical properties, higher porosity, and larger surface area, which are conducive to cell viability, cell

communication, and diffusion of nutrients and oxygen.<sup>19,20</sup> Although fibrous scaffolds have been reported to facilitate the formation of 3D cell spheroids, the resulting spheroids do not have a controllable and uniform size.<sup>21,22</sup> Since spheroid size contributes significantly to spheroid function and obtaining consistent results, several studies have attempted to develop fiber-based microwells by incorporating micropatterned structures into fibers.<sup>21,23</sup> However, these studies only demonstrated the formation of spheroids that adhered to the fibrous microwells; the retrieval of resultant spheroids with uniform size from fiber-based microwell scaffolds and their subsequent delivery to damaged tissue have not been reported.

Previously, our group fabricated fiber-based microwell scaffolds by incorporating hydrogel microstructures into electrospun nano/microfibers and used them to obtain function-enhanced salivary gland stem cell (SGSC) spheroids.<sup>19</sup> However, to deliver SGSCs into irradiated salivary glands, SGSC spheroids should be dissociated into single cells via enzymatic treatment or mechanical dissociation to account for their strong attachment to nanofibers at the bottom of the well. Although the therapeutic efficacy of dissociated SGSCs could be maintained even after their implantation, it would be beneficial to harvest spheroids without enzymatic or mechanical dissociation. Poly(N-isopropylacrylamide) (pNIPAAm)-based thermoresponsive substrates have been widely used for the retrieval of adhesive cells without trypsinization in two-dimensional (2D) cultures because they exhibit cell-adhesive hydrophobic and cell-repellent hydrophilic characteristics at temperatures above and below the lower critical solution temperature (LCST), respectively.<sup>20</sup> This thermoresponsive feature of pNIPAAm-coated substrates has been exploited for cell sheet engineering, in which confluent cells can be detached as one cell sheet when the temperature is lowered without disrupting the cells into single cells.<sup>21–23</sup> Most thermoresponsive substrates for cell retrieval, however, are fabricated in the form of 2D scaffolds, and few examples have been applied to fibrous scaffolds.<sup>24</sup>

In this study, we fabricated thermoresponsive fiber-based microwell scaffolds through a combination of electrospinning and hydrogel patterning and investigated their ability to facilitate the production of 3D cell spheroids of uniform size and the retrieval of cultured spheroids without changes in their forms and functions before their implantation *in vivo*. The thermoresponsive fiber-based microwells enabled the formation of uniform-sized spheroids at temperatures above the LCST. A subsequent decrease in the temperature to a value lower than the LCST enabled the retrieval of SGSC spheroids in a cell-friendly manner. After the SGSC-derived 3D spheroid (SGSC<sup>spheroid</sup>) cells were retrieved, they were implanted into the submandibular glands of mice at 2 weeks post-irradiation. After the delivery of SGSC<sup>spheroid</sup> cells, we evaluated their therapeutic efficacy in an irradiation-induced salivary damage mouse model. In this study, we demonstrated that the stem cell properties of SGSCs

cultured as spheroids within thermoresponsive microwells can be enhanced *in vitro*, and their regenerative potential after implantation can be promoted *in vivo*, compared with those observed in a PBS control group and SGSC monolayer (SGSC<sup>monolayer</sup>) cells.

## Experimental section

### Materials

Polycaprolactone (PCL; MW 80,000), poly(ethylene glycol) diacrylate (PEG-DA 575; MW 575), poly(N-isopropylacrylamide) (pNIPAAm; MW 40,000), 2-hydroxy-2-methylpropionophenone (HOMPP), chloroform, N,N-dimethylformamide (DMF), 2,2,2-trifluoroethanol (TFE), 3-(4,5-dimethylthiazol-2-yl)-2,5-diphenyltetrazolium bromide (MTT), dimethyl sulfoxide (DMSO), phosphate-buffered saline (PBS; pH 7.4), alginate acid, and calcium chloride were purchased from Sigma-Aldrich (Milwaukee, WI, USA). Dulbecco's modified Eagle's medium (DMEM) with 1.0 g/L glucose, Dulbecco's modified phosphate-buffered saline (DPBS), fetal bovine serum (FBS), penicillin/streptomycin (P/S), trypsin/ethylenediaminetetraacetic acid (trypsin/EDTA), acetoxymethyl calcein (calcein-AM), and ethidium homodimer-1 (EthD-1) were purchased from Thermo Fisher Scientific (Waltham, MA, USA).

### Preparation of thermoresponsive fibrous sheets

Fibrous PCL sheets were prepared via electrospinning (NanoNC, Seoul, Korea) under the conditions mentioned in our previous study.<sup>20</sup> Briefly, PCL was dissolved in TFE in a 20% w/v ratio, and the final solution was electrospun by applying a voltage of 7.5 kV to a 23G metallic needle at a constant flow rate of 0.7 mL/h. To prepare the thermoresponsive fibrous sheets, we prepared an electrospinning solution composed of 20% (w/v) polymeric content, with PCL and pNIPAAm mixed at a 1:1 weight ratio. The polymers were dissolved in a mixture of chloroform and DMF at a 3:2 ratio, transferred onto a continuously stirred hotplate overnight at a constant temperature of 60°C, and then loaded into a syringe assembled with a 23G needle. Electrospinning was performed at a positive voltage of 13 kV for 30 min at a constant projection speed of 1 mL/h.

### Fabrication of thermoresponsive fiber-based microwells

The thermoresponsive fibrous sheet was processed through a photolithographic patterning procedure to obtain the microwell structures. A PEG-DA precursor solution, consisting of 50% PEG-DA in the aqueous phase and 2% HOMPP, was first cast on a fibrous sheet before a photomask was placed on top. The photomask was designed to generate 200  $\mu\text{m}$ -sized microwells distanced 100  $\mu\text{m}$  from each other. Exposure to 300 mW/cm<sup>2</sup> of ultraviolet (UV)

light at 365 nm (UV spot lamp; EFOS Ultracure 100ss Plus, Mississauga, Ontario, Canada) for 1 s resulted in the formation of thermoresponsive fiber-based microwell scaffolds. The scaffolds were washed with distilled water to remove unreacted monomers before further use.

### Characterization of thermoresponsive fiber-based microwells

The fibrous sheet morphology was analyzed using a scanning electron microscope (SEM; JSM-7001F, JEOL Ltd., Tokyo, Japan). Samples were prepared prior to imaging by sputter coating them with platinum for 120 s, and images were obtained at an acceleration voltage of 10 kV. The scaffolds were also analyzed using Fourier-transform infrared spectroscopy (FT-IR; Vertex 70, Bruker, Billerica, MA, USA) and an X-ray photoelectron spectrometer (XPS; K-alpha, Thermo Fisher Scientific, Waltham, MA, USA) to confirm the successful incorporation of pNIPAAm into the fibrous mats. FT-IR was performed in the attenuated total reflection mode within a range of 4000–400 cm<sup>-1</sup>. The thermoresponsiveness of the sheets was confirmed by measuring the contact angle using a water droplet (Phoenix-MT(T), SEO, Suwon, Korea).

### Salivary gland stem cell culture

We previously established single ectomesenchymal SGSC clones isolated from human parotid glands using a modified subfractionation culturing method that has been demonstrated to be effective for the isolation of highly homogenous clonal stem cells.<sup>25</sup> After obtaining informed consent and institutional IRB approval (permission number #2015-10-001), human SGSCs were prepared from normal samples of patients who underwent parotidectomy due to a benign parotid tumor. All experimental procedures were performed in accordance with institutional guidelines and regulations. For this experiment, cryopreserved single-clone SGSCs stored in liquid nitrogen vapor were thawed and re-cultured in standard DMEM supplemented with 10% FBS, 100 U/mL penicillin, and 100 mg/mL streptomycin at 37°C with 5% CO<sub>2</sub>. The expanded SGSCs maintained fibroblast-like morphological consistency and constantly proliferated during subculture. SGSCs shown to have stem cell potential, such as self-renewal, tri-lineage differentiation, and sphere forming ability, as described in our previous study, were used in subsequent experiments.<sup>25</sup>

### Culture of salivary gland stem cells into spheroids and retrieval of spheroids from thermoresponsive fiber-based microwells

SGSCs at passage 3 were expanded and seeded at a density of  $1 \times 10^5$  cells/plate. The plates had either been pre-covered with thermoresponsive microwell sheets for SGSC

spheroid culture or were used without a microwell sheet for SGSC monolayer culture. Before the cells were seeded onto scaffolds for spheroid formation, the scaffolds were prepared by washing them with 70% v/v ethanol three times and sterilizing them under UV light for 1 h. Subsequently, trypsinized cells resuspended in growth media after centrifugation were seeded onto the sterilized scaffolds at a concentration of  $1 \times 10^5$  cells/microwell in the 24-well plate. A drop of cell suspension on the scaffold was incubated for at least 1 h at 37°C before submerging the entire scaffold completely in a cell culture medium to further culture the cells. The cells were cultured on scaffolds for the next 5 days until spheroids were uniformly formed in each microwell throughout the scaffold. After SGSC-derived spheroids were completely formed on scaffolds, the culture media were discarded and replaced with cold growth media that had been stored at 4°C. A subsequent decrease in temperature to a value lower than the LCST enabled the retrieval of SGSC spheroids without enzymatic or mechanical dissociation. The scaffolds were placed on a shaking plate for 30 min, and spheroids were retrieved by collecting the entire media in which the scaffolds had been immersed.

### Cell proliferation test and live/dead assay

Cell viability was investigated using two different methods, including MTT assay and fluorescence live/dead assay. MTT assay was utilized to monitor cell proliferation and provide quantitative results reflective of cell viability. A solution consisting of 5 mg/mL of MTT salt was added as 10% v/v in culture medium, and the cells were incubated for 1 h at 37°C. After incubation, the culture medium was completely removed, and purple-colored formazan crystals were dissolved in DMSO and then analyzed using a spectrophotometer (Molecular Devices, San Jose, CA, USA) at 570 nm. Meanwhile, fluorescence live/dead assay was used to obtain qualitative cell viability results. To perform a live/dead assay, we first washed the scaffolds with pre-warmed DPBS twice and then immersed them in a DPBS-based solution containing 2  $\mu$ M calcein-AM and 4  $\mu$ M EthD-1. After incubating the scaffolds for 1 h at 37°C, they were thoroughly washed with DPBS before images were obtained under an inverted fluorescence microscope (Olympus Corporation, Tokyo, Japan). Since calcein-AM and EthD-1 stain live cells and dead cells as green and red, respectively, we could easily obtain qualitative results of cell viability, as well as the locations of live and dead cells, by simply observing fluorescence images.

### Quantitative real-time polymerase chain reaction (qPCR)

To examine the gene expression levels of SGSCs cultured in thermoresponsive microwells, total RNA was extracted

using TRIzol reagent (Invitrogen, Carlsbad, CA, USA), and 500 ng–1  $\mu$ g of total RNA was subjected to first-strand cDNA synthesis (Takara Bio, Shiga Ontario, Japan), according to the manufacturer's instructions. The sequences of primers purchased from OriGene (Rockville, MD, USA) are listed in Table 1. Glyceraldehyde 3-phosphate dehydrogenase was used as an internal control. Real-time PCR was performed using the SYBR Green Lo-ROX qPCR kit (Bioline, Cincinnati, OH, USA) and the QuantStudio™ 5 System (Thermo Fisher Scientific, Waltham, MA, USA). Sample quantification was performed according to the threshold cycle using the  $\Delta\Delta$ Ct method. The values presented in the graphs are mean  $\pm$  SD values.

### Animal experiments and irradiation experiment

All experiments involving animals were approved by the Institutional Animal Care and Use Committee at Yonsei University College of Medicine and conformed to the Avison Biomedical Research Center guidelines (Approval number: 2017-0092). We purchased 7–8-week-old female C3H mice, with an average body weight of 19–21 g (Orientbio, Seongnam, Republic of Korea), and provided them food and water ad libitum. Forty mice were randomly divided into four groups with five mice per group at each time point: non-irradiation + PBS (Sham), irradiation + PBS-injected (PBS), irradiation + SGSC<sup>monolayer</sup>-implanted (SGSC-M), and irradiation + SGSC<sup>spheroid</sup>-implanted (SGSC-S) groups. The mice were irradiated on the neck area with fractionated X-ray radiation at a dose of 7.5 Gy/day for three consecutive days (X-rad 320, Precision X-ray, North Branford, CT, USA). Two weeks after irradiation, the mice were anesthetized via intraperitoneal administration of Zoletil® (50 mg/kg, Virbac, Nice, France) and Rompun® (5 mg/kg, Bayer HealthCare, Mississauga, Ontario, Canada). After the head and neck surface area was sterilized, the submandibular glands (SMGs) were exposed via a 1–2 cm incision on the neck. Each mouse gland was implanted with the same volume (20  $\mu$ L) of implant beneath the capsule of the SMG using a Hamilton syringe. Before transplanting cells into the submandibular gland, we counted the cells of the representative group using trypsin to form a single cell suspension. Next, we administered  $1 \times 10^5$  SGSC<sup>monolayer</sup> cells resuspended in 20  $\mu$ L of PBS in the SGSC-M group and SGSC<sup>spheroid</sup> corresponding to  $1 \times 10^5$  cells in the SGSC-S group. The incision was closed using in vivo auto-clip sutures (Agnthos, Liningo, Sweden). The mice were caged for 16 weeks after irradiation, and their body weights were checked weekly.

### Evaluation of salivary gland function

Body weights were measured during follow-up, and the extirpated gland weight was compared among groups at 4–16 weeks post-irradiation. Before extirpation, mice were anesthetized using Zoletil and Rompun and then

**Table I.** PCR primers used in this study.

Primer	Sequence (5'–3')
LGR4	Forward: GGA GCA TTT GAT GGT AAT CCA CTC Reverse: CCA TGC TTG CAC CAC GAA TGA C
LGR5	Forward: CCT GCT TGA CTT TGA GGA AGA CC Reverse: CCA GCC ATC AAG CAG GTG TTA A
LGR6	Forward: GAG ATG GAG GAC TCA AAG CC A Reverse: AGT CCA TTG CAG AGC ACG GAG A
SOX2	Forward: GCT ACA GCA TGA TGC AGG ACC A Reverse: TCT GCG AGC TGG TCA TGG AGT T
NANOG	Forward: CTC CAA CAT CCT GAA CCT CAG C Reverse: CGT CAC ACC ATT GCT ATT CTT CG
FGF1	Forward: TAA AAG CCC GTC GGT GTC CAT G Reverse: ATG GCA CAG TGG ATG GGA CAA G
FGF2	Forward: AGC GGC TGT ACT GCA AAA ACG G Reverse: CCT TTG ATA GAC ACA ACT CCT CTC
FGF10	Forward: TAG GAA GAA CGC GAA GGT CAG C Reverse: TGG CTT TGA CGG CAA CAA CTC C
EGF	Forward: TGC GAT GCC AAG CAG TCT TGT A Reverse: GCA TAG CCC AAT CTG AGA ACC AC
HGF	Forward: CAA TGC CTC TGG TTC CCC TT Reverse: CCC TTG TAG CTG CGT CCT TT
IGF-1	Forward: CTC TTC AGT TCG TGT GTG GAG AC Reverse: CAG CCT CCT TAG ATC ACA GTC C
BDNF	Forward: CAT CCG AGG ACA AGG TGG CTT G Reverse: GCC GAA CTT TCT GGT CCT CAT C
GAPDH	Forward: GTC TCC TCT GAC TTC AAC AGC G Reverse: ACC ACC CTG TTG CTG TAG CCA A

BDNF: brain derived neurotrophic factor; EGF: epidermal growth factor; FGF: fibroblast growth factor; GAPDH: glyceraldehyde-3-phosphate dehydrogenase; HGF: hepatocyte growth factor; IGF: insulin growth factor; LGR: leucine-rich repeat-containing G-protein coupled receptor; NANOG: homeobox protein; SOX2: sex determining region Y.

intraperitoneally administered with muscarinic agonist pilocarpine (2 mg/kg) to stimulate saliva secretion. Saliva was collected from the floor of the mouth using a micropipette 3 min after stimulation. The collected saliva was placed in pre-weighed 1.5-mL microcentrifuge tubes, and salivary flow rate (SFR) ( $\mu\text{L}/\text{min}/\text{mg}$ ) was calculated by dividing the volume ( $\mu\text{L}$ ) of the total collected saliva by the collection time (min) and weight of SMGs (mg). Saliva production ratio was calculated as the SFR of each group relative to the SFR of the sham group. Salivary lag time(s) was defined as the time from stimulation to the beginning of saliva secretion.

### Tissue histology

At 4 and 16 weeks after irradiation, SMGs were extirpated, fixed, and paraffin-embedded. Paraffinized samples were cut into 2- $\mu\text{m}$  thick sections before they were deparaffinized and stained using hematoxylin and eosin (H&E) (ab245880, Abcam), Masson's trichrome (MTC, ab150686, Abcam), and periodic acid–Schiff (PAS) (ab150680, Abcam) staining according to the manufacturers' instructions. Two blinded examiners assessed the pathological

changes, including mucin intensity (PAS), structure (H&E), and fibrosis (MTC). SMG damage was quantified based on morphological breakdown of acinar and ductal structures after H&E staining. Staining scores were recorded as 0–5 based on the following criteria: staining intensity was scored as 1 for 5% or less, 2 for 5%–20%, 3 for 20%–50%, 4 for 50%–80%, and 5 for 80% or more stained cells.<sup>26</sup> Degrees of fibrosis were determined by MTC staining, which indicated the connective tissue compartment (inherent fibrotic lesion) in blue. The area of mucin production in acini was measured as the ratio of mucin (magenta) and others (blue) through PAS staining. Two blind examiners scored SMG structural damage and measured the ratio of mucin-containing area.

### TUNEL assay

Apoptotic cells in SMG tissues were analyzed using terminal deoxynucleotidyl transferase-mediated dUTP nick-end labeling (TUNEL) staining using an apoptotic cell detection kit (Millipore, Billerica, MA, USA) at 37°C for 60 min in the dark according to the manufacturer's instructions. Cells were counterstained for 5 min

**Table 2.** Antibodies used in this study.

	Antibody	Dilution	Host	Provider
Acinar	MIST1	1:500	Rabbit	Abcam
	AQP5	1:1000	Rabbit	Alomone
Ductal	KRT7	1:200	Mouse	Abcam
Apoptotic	CASP3	1:500	Mouse	Cell Signaling
	$\gamma$ H2AX	1:300	Mouse	Cell Signaling
Proliferation	Ki67	1:300	Mouse	DB Science
Cell tracing	GFP	1:500	Rabbit	Novus

AQP5: aquaporin-5; CASP3: caspase-3; GFP: green fluorescent protein; Ki67: cellular marker for proliferation; KRT7: keratin 7; MIST1: Class A basic helix-loop-helix protein 15;  $\gamma$ H2A.X: DNA repair protein.

using DAPI (Vector Labs, San Diego, CA, USA). TUNEL-positive cells had pyknotic nuclear fragments that were stained dark green after fluorescent staining of apoptotic cells. Apoptotic cells were quantified by assessing the number of TUNEL-positive cells from three randomly selected fields per slide from each mouse using a blinded examiner. All fluorescence images of the sections were obtained using an Axio Imager M2 microscope (Carl Zeiss).

### Immunohistochemistry and immunofluorescence

Formalin-fixed paraffin-embedded tissue sections were dewaxed in xylene, rehydrated with distilled water, and immunofluorescence-stained using a heat-induced epitope retrieval buffer (HIER, Tris-EDTA, pH 9.0), with 5% normal goat serum as the blocking solution. Subsequently, the slides were washed in tris-buffered saline before incubating tissue sections with primary antibodies against KRT7 (BioLegend, San Diego, CA, USA), AQP5 (Alomone, Jerusalem, Israel), Ki67 (Abcam), MIST1 (Abcam), GFP (Abcam), cleaved caspase-3 (Cell Signaling), and  $\gamma$ H2AX (Cell Signaling) diluted in blocking solution. Sections were incubated overnight at 4°C, washed in tris-buffered saline, and incubated with the corresponding secondary antibodies conjugated biotinylated secondary antibodies with horseradish peroxidase and 3,3'-diaminobenzidine or Alexa Fluor (Invitrogen) for 60 min at room temperature in the dark. Sections were washed in tris-buffered saline, treated with May's hematoxylin or DAPI (Vector Labs, San Diego, CA, USA), allowed to air dry, cover-slipped, and processed for observation under an Axio Imager M2 (Carl Zeiss, Jena, Germany) microscope. For quantification of double-labeled cells, three random areas were chosen within each section from at least five glands per group. Total numbers of MIST1<sup>+</sup> mature acinar cells, KRT7<sup>+</sup> terminally differentiated luminal ductal cells, TUNEL<sup>+</sup> dead cells, and AQP5<sup>+</sup> proacinar cells double labeled with CC3,  $\gamma$ H2AX, and Ki67 were counted using ImageJ (National Institutes of Health, USA). Information on the dilutions of the antibodies is provided in Table 2.

### Data analysis

All experiments were performed in triplicate. Statistical analysis was performed using Prism software (GraphPad® Software, Inc., CA, USA), and statistical significance was defined as \* $p < 0.05$ , \*\* $p < 0.01$ , \*\*\* $p < 0.001$  for comparison to Sham; ### $p < 0.01$ , #### $p < 0.001$  for comparison to PBS (irradiation); and \$\$\$ $p < 0.01$  for comparison to SGSC-M. \*One-way ANOVA and Tukey's post hoc test were used to compare groups.

## Results

### Fabrication of thermoresponsive fiber-based microwells

Thermoresponsive scaffolds were fabricated through electrospinning of thermoresponsive polymers, followed by photolithographic patterning of PEG hydrogel (Figure 1). A fibrous mat based on the thermoresponsive polymer was obtained by electrospinning a pNIPAAm and PCL mixture.

The photographic images shown in Figure 2(a) indicate that there were no differences in the overall appearances of bare PCL fibers and thermoresponsive fibers incorporating pNIPAAm. SEM images also indicated that the fibrous structure with a smooth surface was maintained effectively in the thermoresponsive fibrous mat as well as PCL fibrous sheets. The average diameter of pNIPAAm/PCL-blended thermoresponsive fibers ( $1.42 \pm 0.55 \mu\text{m}$ ) was slightly lower than that of bare PCL fibers ( $1.75 \pm 0.12 \mu\text{m}$ ). The stability of thermoresponsive PCL/pNIPAAm blended fibrous sheets was investigated by observing fibrous morphology through SEM. As shown in Supplemental Figure S1, the characteristic fibrous structure was maintained even after submerging the blended fibrous sheets in PBS for 24 h at different temperatures (25°C–37°C). The stability of the thermoresponsive fibers was further verified through reversibility of the contact angle after 24 h. As shown in Supplemental Figure S2, the contact angles measured at two different temperatures (25°C–37°C), which were chosen based on the LCST of pNIPAAm, were maintained within a reasonable range through seven cycles of temperature changes.

Owing to differences in the chemical compositions of PCL and pNIPAAm, the presence of pNIPAAm in the thermoresponsive fibrous mat was confirmed by both XPS and FT-IR: PCL is a polyester consisting of carbon and oxygen, while pNIPAAm has a branched carbonyl group that extends from the backbone. This carbonyl group contains a secondary amine with an isopropyl group at the end. The XPS spectra for pure PCL and blended pNIPAAm/PCL fibers both indicated peaks at approximately 530 and 280 eV, which represented oxygen and carbon, respectively. However, the XPS spectra of the blended fibers exhibited a small peak at 400 eV, representing nitrogen, which was clear evidence for the

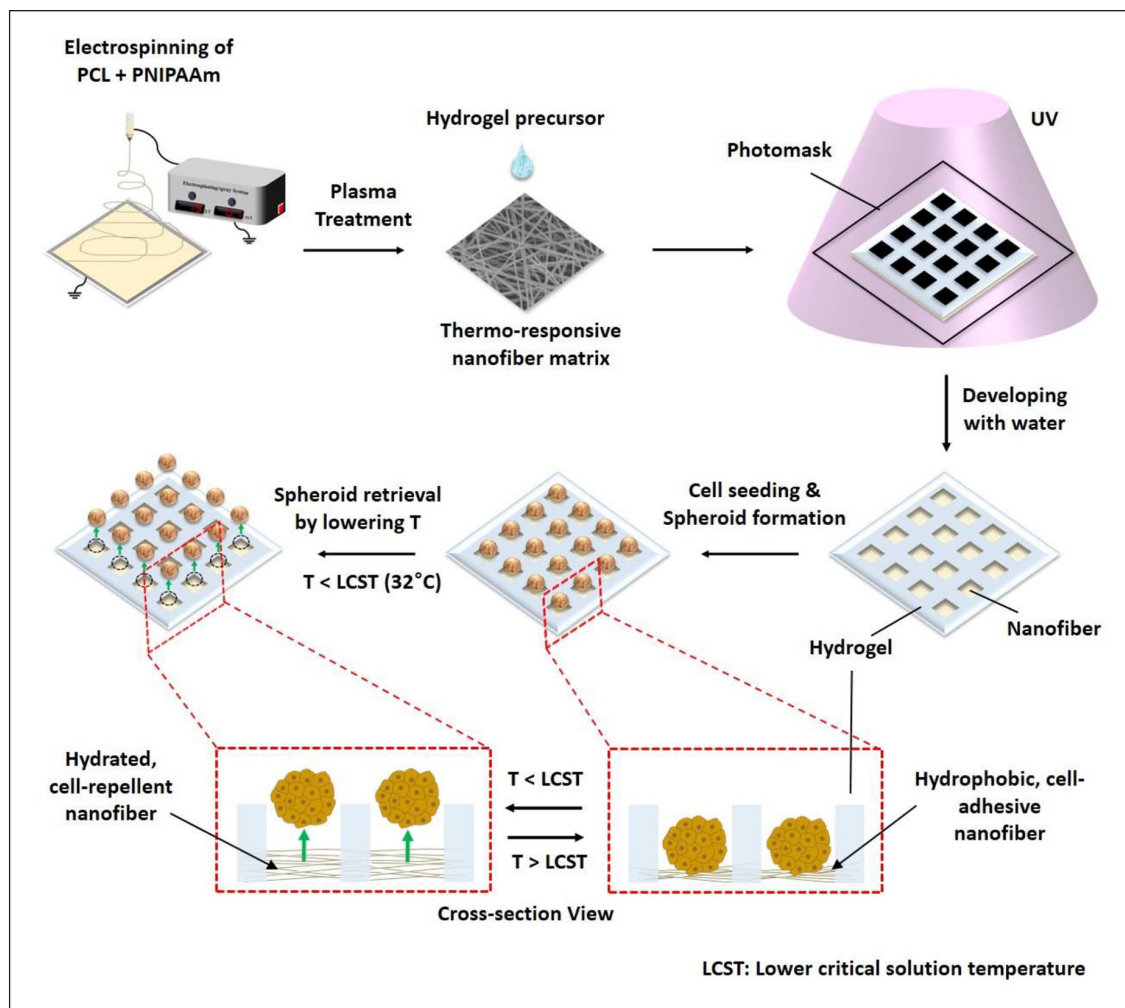


**Figure 1.** Schematic representation of the fabrication of thermoresponsive microwells through electrospinning and photolithographic patterning of polyethylene glycol (PEG) hydrogel and culture and retrieval of SGSC spheroids from thermoresponsive microwells.

presence of a primary amine group in pNIPAAm (Figure 2(b)).<sup>24</sup> The atomic % of C, N, and O was 76.9%, 4.4%, 18.7%, respectively. Using the atomic ratio, we could calculate the weight percentage of pNIPAAm on the outmost layer of thermoresponsive fibers, as described in a previous study.<sup>24</sup> The surface concentration of pNIPAAm was 34.2%. In the FT-IR graphs (Figure 2(c)), the spectra comprised peaks at  $1047\text{ cm}^{-1}$  (C-C stretch),  $962\text{ cm}^{-1}$  (methyl group), and  $1724\text{ cm}^{-1}$  (carbonyl group), whereas peaks at  $1460\text{ cm}^{-1}$  ( $\text{CH}_3$  asymmetrical deformation),  $1543\text{ cm}^{-1}$  (secondary amine, N-H deformation), and  $1647\text{ cm}^{-1}$  (amide I) were observed for the blended fibers alone. Moreover, a slightly higher absorbance in the range of  $900\text{--}1000\text{ cm}^{-1}$  for the blended fibers indicated that the incorporation of pNIPAAm increased the number of methyl groups.<sup>27,28</sup> The thermoresponsive properties of the pNIPAAm/PCL fibers were additionally investigated by analyzing the contact angle of a water droplet on the surface of the fibrous sheet. Because the

LCST of pNIPAAm is  $32^\circ\text{C}$ , the contact angle of the water drop was measured at two different temperatures, each representative of temperatures below and above the LCST. The contact angle at the higher temperature ( $40^\circ\text{C}$ ) was approximately  $90^\circ$ , but decreased to  $37^\circ$  after 10 s when the temperature was below the LCST ( $25^\circ\text{C}$ ) (Figure 2(d)). After the preparation of pNIPAAm/PCL fibers, PEG hydrogel micropatterns were incorporated into the fibers to create fibrous microwell arrays consisting of cell-adhesive fiber bottoms and cell-repellent hydrogel walls (Figure 2(e)).

#### *Culture of SGSCs in thermoresponsive microwells and stem cell function of SGSC spheroid cells*

SGSCs were seeded on thermoresponsive fiber-based microwell scaffolds to form spheroids. Fluorescence images were obtained using a fluorescence microscope at

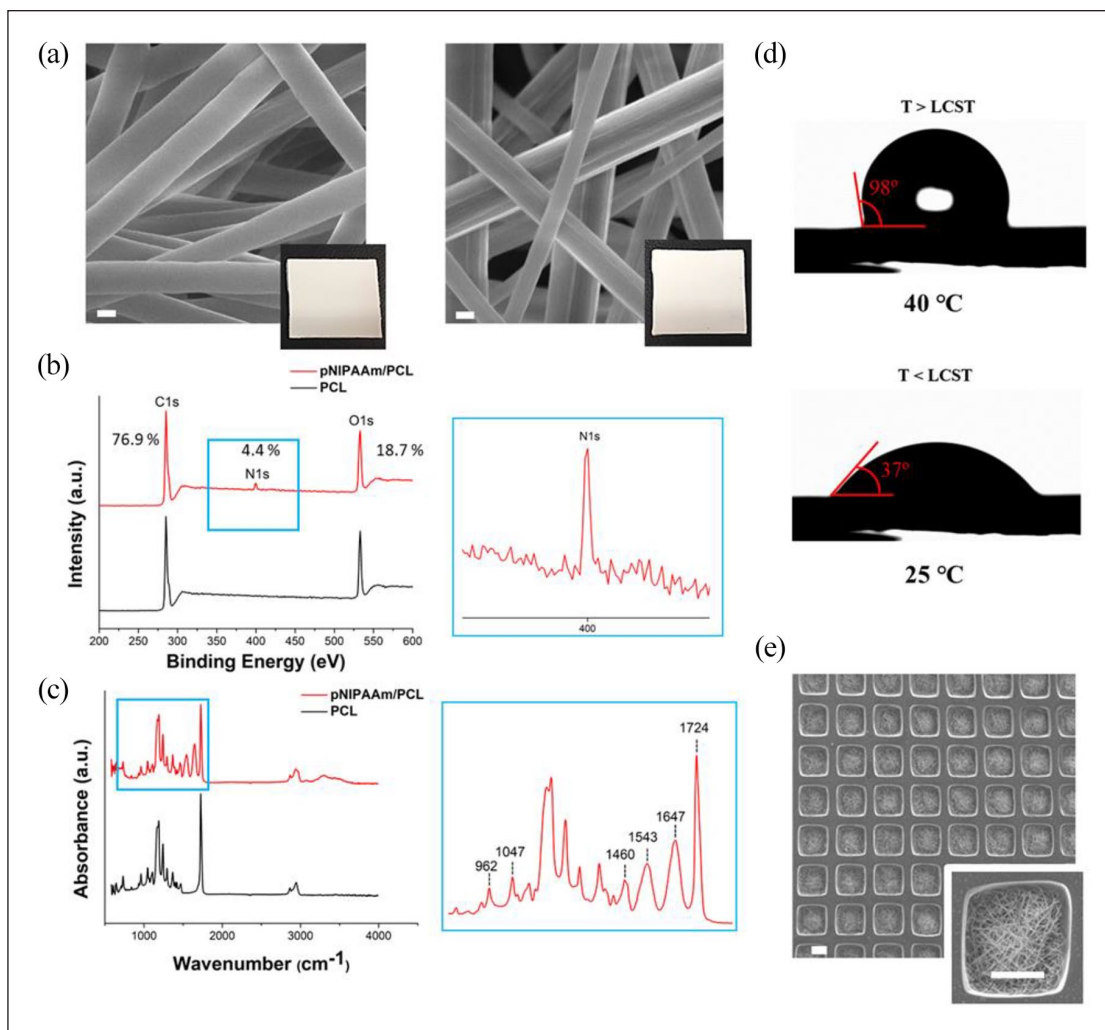


**Figure 2.** Characterization of fibrous sheets fabricated through electrospinning. The morphology and chemical composition of bare PCL fibers (left) and pNIPAAm/PCL blended thermoresponsive fibers (right) were characterized using (a) SEM, (b) XPS, and (c) FT-IR (scale bar = 1  $\mu\text{m}$ ). (d) The thermoresponsiveness of the pNIPAAm/PCL-blended fibrous sheets was verified by measuring the contact angle at a temperature below (top) and above (bottom) the lower critical solution temperature (LCST) of pNIPAAm. (e) SEM image of thermoresponsive microwells (scale bar = 100  $\mu\text{m}$ ).

day 5 of culture, immediately after the live/dead assay, in which living cells were stained green and dead cells were stained red (Figure 3(a)). The microscopic images confirmed the formation of spheroids. Strong green fluorescence from SGSCs indicated that the cells remained viable after spheroid formation. The viability of cells was also observed over the course of 7 days via MTT assay, and as shown in Figure 3(b), the relative viability of cells on pNIPAAm/PCL-based microwells was approximately 100% throughout the culture period ( $97\% \pm 2.3\%$ ), compared with the control condition on PCL-based microwells. Next, we conducted quantitative PCR to examine changes in stemness and paracrine factor gene expression levels. When we first compared the gene expression of 2D SGSCs dissociated with trypsin (SGSC-M), 3D SGSC spheroids detached by trypsinization (SGSC-T), and SGSC<sup>spheroid</sup>

cells (SGSC-S), we found that the mRNA levels of the trypsinized SGSCs in the SGSC-M and SGSC-T groups were lower than those of SGSC<sup>spheroid</sup> cells in the SGSC-S group (Figure 3(c)). The expression of stem cell-related genes (*LGR4*, *LGR5*, *LGR6*, *SOX2*, and *NANOG*) was upregulated in SGSC<sup>spheroid</sup> cells, relative to that observed in SGSC<sup>monolayer</sup>, and the levels of *LGR4*, *LGR5*, and *LGR6* gene expression were significantly higher than those in trypsinized SGSC<sup>spheroid</sup> cells, indicating that stemness was enhanced and maintained after 3D spheroid culture using thermoresponsive microwells. Paracrine activity was also enhanced in SGSC<sup>spheroid</sup> cells, along with the expression of more mitogenic (*EGF*), anti-apoptotic (*IGF-1* and *HGF*), or morphogenic (*FGF1* and *FGF2*) growth factor genes, compared to SGSC<sup>monolayer</sup> cells. However, the morphogenic factor *FGF10* and neurotrophic factor *BDNF*



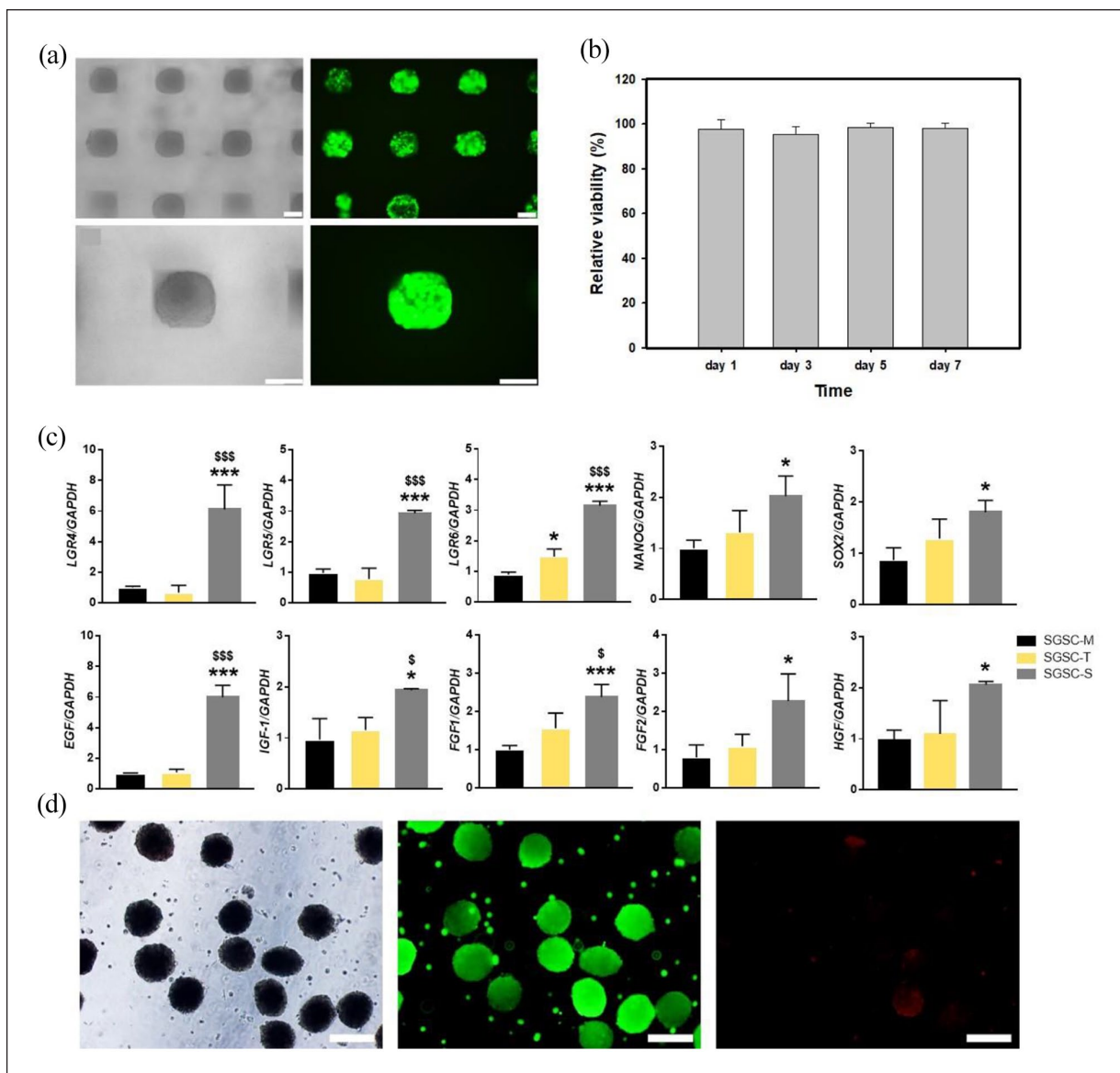


**Figure 3.** Thermo-responsive microwells facilitate spheroid formation and retrieval. (a) Spheroids were qualitatively observed using brightfield and fluorescent microscopes after calcein-AM (green) and EthD-1 (red) staining in live/dead assay (scale bar = 100 μm). (b) Relative viability of SGSCs on thermo-responsive microwells compared with that in bare PCL microwells during 7 days of spheroid formation. (c) Changes in expression levels of stem cell-related genes (*LGR4*, *LGR5*, *LGR6*, *SOX2*, and *NANOG*) and mitogenic (*EGF*), anti-apoptotic (*IGF-1* and *HGF*), or morphogenic (*FGF1* and *FGF2*) growth factors were analyzed using qRT-PCR at 5 days after culture. SGSC-M: SGSC<sup>monolayer</sup> group; SGSC-T: trypsinized SGSC<sup>spheroid</sup> group; SGSC-S: SGSC<sup>spheroid</sup> group. (d) The qualitative live/dead assay for spheroids was performed immediately after detachment at 5 days after culture on the microwells (scale bar = 200 μm).

were not significantly upregulated in SGSC<sup>spheroid</sup> cells, compared with SGSC<sup>monolayer</sup> cells (Data not shown). Expression of *EGF*, *IGF-1*, and *FGF1* was significantly higher than that in trypsinized SGSC<sup>spheroid</sup> cells.

### Spheroid retrieval from microwells

The microscopic images shown in Figure 3(d) demonstrate that SGSC<sup>spheroid</sup> maintained their spherical shape

and viability after detachment from the scaffold. Green fluorescence emitted from the spheroids confirmed their viability after detachment. The efficiency of spheroid retrieval, which was defined as the number of retrieved spheroids after detachment divided by the total number of spheroids in scaffolds before detachment, was approximately 82% (82% ± 22%). The size of the spheroids was uniform and approximately 157 μm in diameter (157 ± 18 μm).

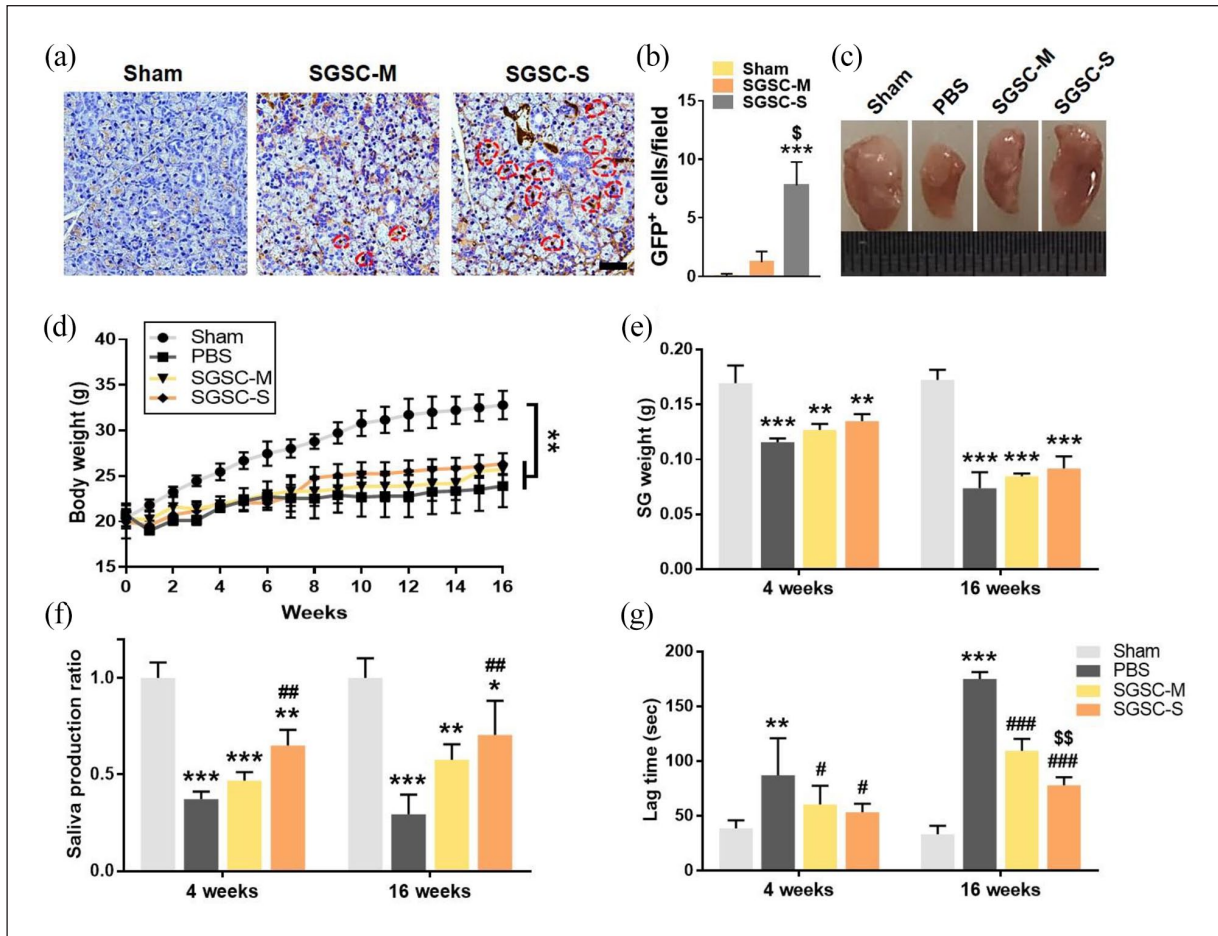


**Figure 4.** Therapeutic effect of SGSCs implanted as spheroids or monolayers on salivary gland hypofunction. (a) Immunostaining to evaluate the distribution of GFP-positive cells (red circle) (scale bar = 50  $\mu$ m). (b) The average numbers of engrafted GFP-positive cells from three random fields per each section at 2 weeks after implantation were compared among Sham, SGSC<sup>monolayer</sup>, and SGSC<sup>spheroid</sup> groups. Three random sections from 3 mice were evaluated ( $n=9$ ). One-way ANOVA using Tukey's post-hoc test was used to compare groups; \*compared with Sham; \$compared with SGSC<sup>monolayer</sup>. (c) Representative macroscopic image of SMGs at 16 weeks after irradiation. (d) Changes in body weight over time after irradiation. (e) Salivary gland weight measured at 4 and 16 weeks after irradiation. (f) Saliva production ratio after stimulation at 4 and 16 weeks after irradiation. (g) Lag time to salivation (s) after pilocarpine stimulation at 4 and 16 weeks after irradiation. One-way ANOVA with Tukey's post hoc test was used to compare groups; \*compared with Sham; #compared with PBS; \$compared with SGSC<sup>monolayer</sup>.  $n=5$  mice per each group. \* $p < 0.05$ , \*\* $p < 0.01$ , \*\*\* $p < 0.001$ , # $p < 0.05$ , ## $p < 0.01$ , ### $p < 0.001$ , \$\$\$ $p < 0.05$ , and \$\$\$ $p < 0.01$ .

### Assessing irradiation-related morbidity and functional changes

For engraftment assay, we labeled SGSCs using green fluorescence protein (GFP) via the transfection of GFP into SGSCs using lentiviral GFP vectors and implanted SGSC<sup>spheroid</sup> cells or SGSC<sup>monolayer</sup> cells into mouse SMGs 2 weeks after fractionated irradiation. At 2 weeks post-implantation (4 weeks post-irradiation), immunohistochemical analysis revealed that more SGSCs were observed in the SGSC<sup>spheroid</sup> group than in the SGSC<sup>monolayer</sup> group (Figure 4(a) and (b)). SMGs were extirpated at 4–16 weeks post-irradiation, and the gross glandular volume appeared to decrease in the PBS group (Figure 4(c)). Irradiation induced weight loss, and the average body

weight of SGSC<sup>spheroid</sup> group mice tended to be higher than that of PBS control mice, although the difference was not statistically significant (Figure 4(d)). The average weights of SMGs significantly decreased after irradiation, and implantation of SGSCs, either as spheroid or monolayer cells, elicited a lower decline in glandular weight, compared with the PBS group, although they did not significantly differ (Figure 4(e)). We also measured the saliva production ratio (SFR of each group relative to the SFR of the sham group) and lag time of salivation to evaluate salivary gland function after irradiation. Irradiation significantly reduced salivation (Figure 4(f)) and delayed the lag time to salivation (Figure 4(g)). The relative saliva production of the SGSC<sup>spheroid</sup> group only exhibited a significant increase, compared with that of

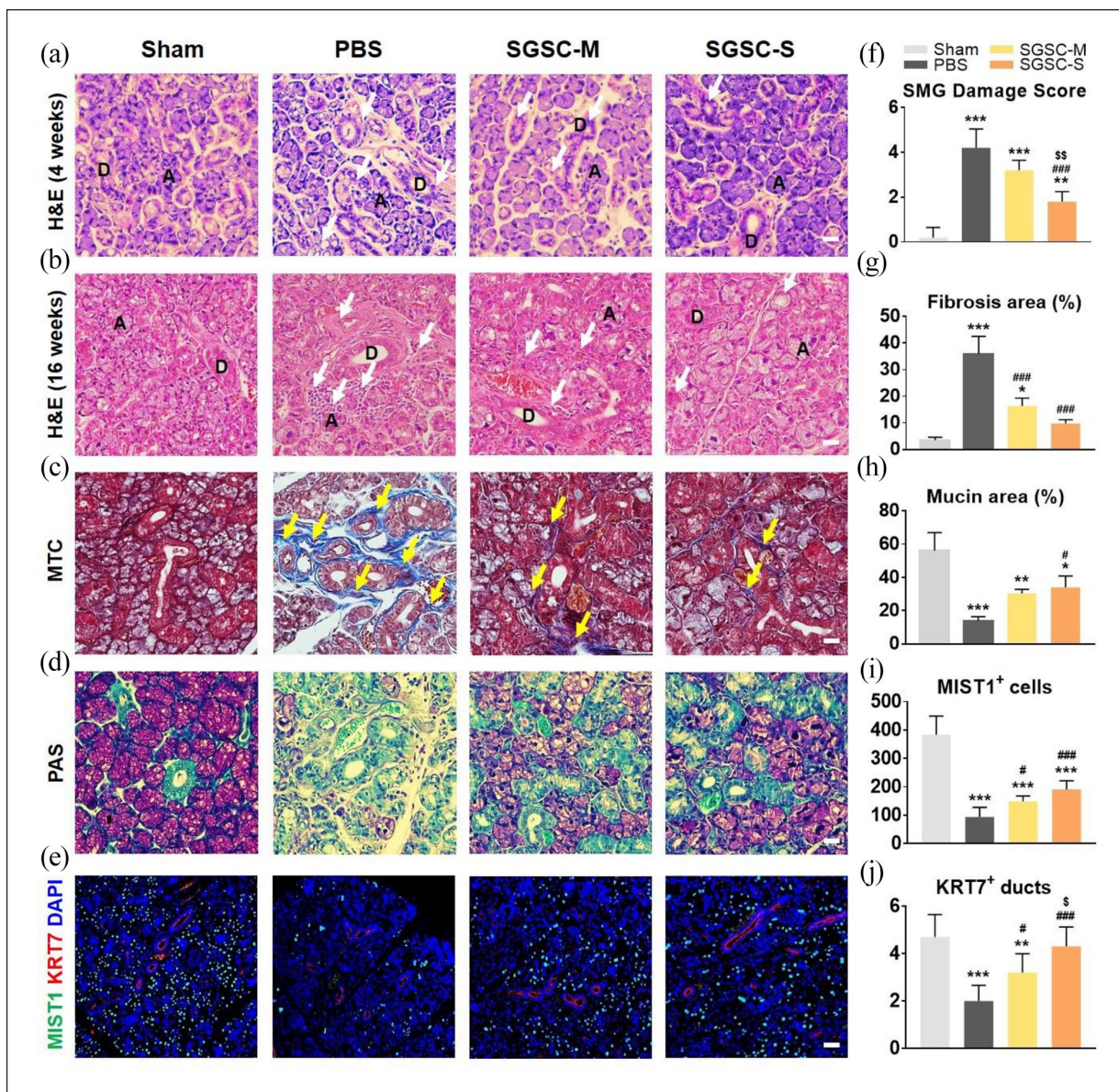


**Figure 5.** Implantation of SGSC<sup>spheroid</sup> or SGSC<sup>monolayer</sup> cells demonstrates radioprotection of salivary gland cells post-irradiation. Representative histological images of H&E staining at (a) 4 weeks and (b) 16 weeks post-irradiation (scale bar = 25  $\mu$ m). Arrows indicate vacuolization. “A” and “D” indicate acinar cells and ductal cells, respectively. (c) MTC and (d) PAS staining at 16 weeks post-irradiation (scale bar = 25  $\mu$ m). Arrows indicate fibrosis. (e) Representative immunofluorescence images of KRT7<sup>+</sup> luminal ductal cells and MIST1<sup>+</sup> acinar cells (scale bar = 50  $\mu$ m). (f) Densitometric analyses were performed by measuring the pixels of the acinar and ductal areas after H&E staining; SMG damage score was quantified based on the morphological breakdown of acinar and ductal structures after H&E imaging, (g) blue fibrotic lesion areas after MTC staining, and (h) magenta mucin areas after PAS staining. The number of (i) MIST1<sup>+</sup> cells and (j) KRT7<sup>+</sup> cells in immunofluorescence images were evaluated by densitometry. All fields used for densitometric analyses were randomly selected three times, and computations were performed using Image J software. Data are presented as the mean cell number  $\pm$  standard error of the mean. One-way ANOVA using Tukey’s post hoc test was used to compare the groups. SGSC-M: SGSC<sup>monolayer</sup>; SGSC-S: SGSC<sup>spheroid</sup>; \*compared with Sham; #compared with PBS; §compared with SGSC<sup>monolayer</sup>.  $n = 5$  mice per each group. \* $p < 0.05$ , \*\* $p < 0.01$ , \*\*\* $p < 0.001$ , # $p < 0.05$ , ### $p < 0.001$ , § $p < 0.05$ , §§ $p < 0.01$ , and §§§ $p < 0.001$ .

the PBS group, at 4 and 16 weeks after irradiation. At 16 weeks after irradiation, the SGSC-treated groups exhibited a decreasing lag time, and the difference in improvement was significantly greater in the SGSC<sup>spheroid</sup>

group than the SGSC<sup>monolayer</sup> group (Figure 4(g)), suggesting that the radioprotective effect might be greater when SGSC<sup>spheroid</sup> cells, instead of SGSC<sup>monolayer</sup> cells, were implanted.

### Micromorphological evaluation of salivary gland structures and composition of salivary epithelial cells

To confirm the structural recovery of salivary glands, we analyzed microscopic changes via H&E, PAS, MTC, and immunofluorescence staining (Figure 5(a)). The results of H&E staining at 4 and 16 weeks post-irradiation revealed that acinar and ductal structures in the SGSC<sup>monolayer</sup> and SGSC<sup>spheroid</sup> groups were more intact than those in the irradiated and PBS-injected groups (Figure 5(a) and Supplemental Figure S3). At 4 weeks after irradiation, we observed microscopic changes, including vacuolization in the acini, widening of ducts, and loosening of the interstitium (Figure 5(a)). At 16 weeks after irradiation, SMG damage was further aggravated, and SMG damage scores quantified based on morphological breakdown of acinar and ductal structures after H&E staining revealed that the SGSC<sup>spheroid</sup>-implanted group experienced a significant amelioration of SMG structures damaged by irradiation, compared with those in the PBS group (Figure 5(b)). Moreover, the average damage score was lower in the SGSC<sup>spheroid</sup> group than in the SGSC<sup>monolayer</sup> group (Figure 5(f)). Degrees of fibrosis were evaluated by measuring blue areas after MTC staining, and mucin-producing acini were assessed by quantification of magenta-colored areas (Figure 5(c) and (d)). The results of morphometric analysis revealed that fibrosis increased and mucin-containing area decreased significantly after irradiation; however, fibrosis decreased and mucin-producing area increased in the SGSC<sup>spheroid</sup>-implanted group, compared with the PBS group (Figure 5(g) and (h)). Immunofluorescence staining results indicated that the number of MIST1<sup>+</sup> acinar-KRT7<sup>+</sup> ductal cells decreased significantly after irradiation, while the number of MIST1<sup>+</sup> cells-KRT7<sup>+</sup> ducts in the SGSC-treated groups was significantly higher than that in the PBS group (Figure 5(e), (i) and (j)). Moreover, the results of densitometric analysis after immunofluorescence staining of KRT7<sup>+</sup> ductal cells also revealed that the regenerative potential of SGSCs was significantly greater in the SGSC<sup>spheroid</sup> cells than the SGSC<sup>monolayer</sup> cells at 16 weeks post-irradiation.

### SGSC spheroids exhibit an enhanced protective effect against irradiation-induced cell death and tissue damage

Next, we examined the mechanisms by which SGSCs preserved the structure and function of SMGs against irradiation. To investigate whether SGSC implantation protected SMG architecture and function by inhibiting cell death, we performed a TUNEL assay and immunofluorescence analysis to detect activated caspase-3. Fractionated irradiation at a dose of 7.5 Gy/day for three consecutive days to the neck induced apoptosis in cells, in which TUNEL-positive

apoptotic cells were markedly increased after irradiation. The number of TUNEL-positive dead cells was significantly decreased in both the SGSC<sup>spheroid</sup> and the SGSC<sup>monolayer</sup> groups, compared with that in the PBS group (Figure 6(a) and (b)). The co-expression of caspase-3, an apoptosis marker with AQP5<sup>+</sup> pro-acinar cells, was observed at 4 weeks post-irradiation, and the number of caspase-3-expressing pro-acinar cells significantly decreased in both the SGSC<sup>monolayer</sup> and SGSC<sup>spheroid</sup> groups (Figure 6(c) and (d)). The levels of the DNA damage marker  $\gamma$ H2AX increased markedly after irradiation, but decreased in both the SGSC<sup>monolayer</sup> and SGSC<sup>spheroid</sup> groups (Figure 6(e) and (f)). These radioprotective effects against irradiation-induced DNA damage-related cell death were significantly greater in the SGSC<sup>spheroid</sup> group than in the SGSC<sup>monolayer</sup> group. Immunofluorescence staining revealed that Ki67 expression levels increased significantly in the AQP5<sup>+</sup> pro-acinar cells only in the SGSC<sup>spheroid</sup> group (Figure 5(g) and (h)). Altogether, these findings suggest that SGSCs provided as 2D monolayer cells or 3D spheroid cells can protect AQP5<sup>+</sup> pro-acinar cells from radiation-induced cell damage, which may contribute to the amelioration of salivary gland damage and deterioration by irradiation.

### Discussion

This study was performed to develop a bioengineering system that would enhance stem cell properties and facilitate the retrieval of spheroids cultured in a 3D thermoresponsive microwell culture format. We found that SGSCs could aggregate to form 3D spheroids when cultured in thermoresponsive microwells. The spheroid cells in the thermoresponsive microwells exhibited higher expression of stemness and paracrine growth factor-related genes, including *LGR4*, *LGR5*, *LGR6*, *EGF*, *IGF-1*, and *FGF1*, than dissociated SGSC<sup>spheroid</sup> cells by trypsinization as well as SGSC<sup>monolayer</sup>. After the implantation of SGSCs, either as spheroids or monolayers, into SMGs after irradiation, we observed that SGSCs could protect against radiation-induced cell death, ameliorate tissue damage, and restore secretory function. Our results also indicated that SGSC<sup>spheroid</sup> cells enhanced anti-apoptotic and regenerative potential, as well as engraftment efficiency, which resulted in the preservation of more salivary epithelial cells and glandular structures at 16 weeks post-irradiation than that observed with SGSC<sup>monolayer</sup> cells. These results indicated that SGSC<sup>spheroid</sup> cells have better therapeutic potential for stimulating recovery from tissue damage and functional deterioration after irradiation than cells forming a monolayer.

Various culture techniques, including those for the generation of synthetic scaffolds that mimic the topographical and mechanical properties of the ECM, have been utilized to regulate salivary gland cell function and/or salivary tissue organization. Several research groups have reported that salivary epithelial cells and/or progenitors incorporated into synthetic

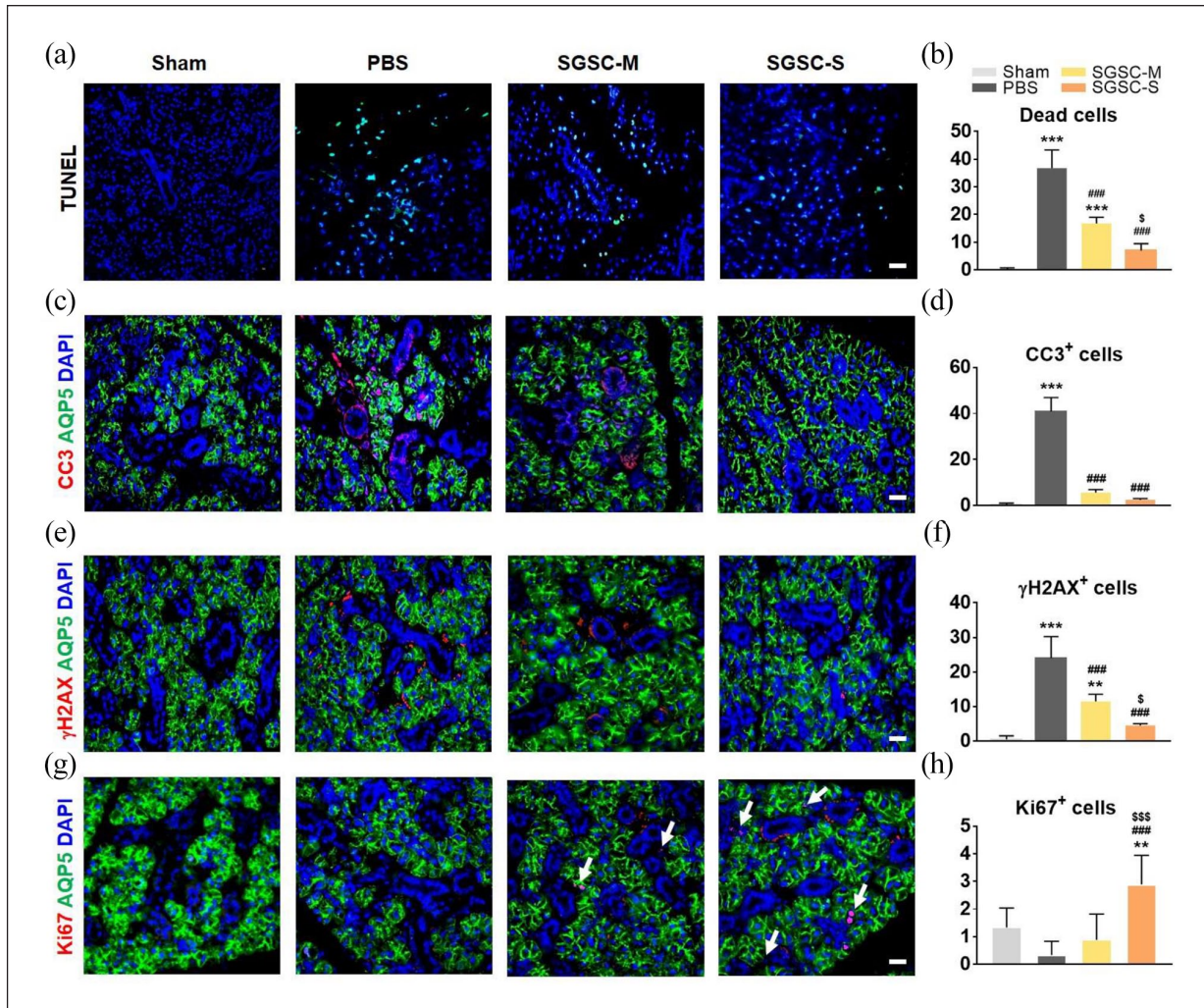


**Figure 6.** SGSC<sup>spheroid</sup> cells exhibiting enhanced anti-apoptotic effects and proliferative activities, compared with those observed for SGSC<sup>monolayer</sup> cells at 4 weeks post-irradiation. (a) Representative images and (b) quantified positive cell numbers were obtained via the TUNEL assay (scale bar = 25 μm). (c) Representative immunofluorescence images and (d) quantified positive CC3 cell number in AQP5<sup>+</sup> cells. The nuclei were counterstained with DAPI (scale bar = 25 μm). (e) Representative immunofluorescence images and (f) quantified positive cell number of γH2AX in AQP5<sup>+</sup> cells. (g) Representative immunofluorescence images and (h) quantified positive Ki67 cell numbers in AQP5<sup>+</sup> cells (white arrow). Three random fields of each section were calculated per mouse via positive cell counting. Data are presented as mean cell number ± standard error of the mean. One-way ANOVA using Tukey's post hoc test was used to compare groups. SGSC-M: SGSC<sup>monolayer</sup>; SGSC-S: SGSC<sup>spheroid</sup>; \*compared with Sham; #compared with PBS; \$compared with SGSC<sup>monolayer</sup>. n = 5 mice per each group. \*\*p < 0.01, \*\*\*p < 0.001, ###p < 0.001, \$p < 0.05, and \$\$\$p < 0.001.

or natural scaffolds using poly(lactic-co-glycolic acid) (PLGA), poly(vinylidene fluoride) (PVDF),<sup>29–31</sup> and PEG<sup>32</sup> or chitosan,<sup>33</sup> fibrin,<sup>34,35</sup> and hyaluronic acid-based hydrogels<sup>36,37</sup> exhibit salivary tissue organization. Biomaterial-based culture processes that facilitate cell-to-cell or cell-to-ECM contact through the embedding or seeding of cells into ECM-based scaffolds<sup>38</sup> or micropatterned nanofibrous scaffolds<sup>39,40</sup> have also been reported to be of potential use for the modulation of salivary cell function. We previously demonstrated that salivary acinar-like organization occurs when epithelial cells from the salivary gland are subjected to spheroid culture in nanofibrous PCL scaffolds with microwells.<sup>41</sup> Recently, we

also demonstrated that 3D cultures enable the priming of cells and enhance the stem cell functions of SGSCs within fibrous microwells.<sup>19</sup>

Electrospinning techniques have provided significant opportunities for the enhancement of cellular functionality. The incorporation of PEG hydrogel onto electrospun fibrous sheets via photolithographic patterning has resulted in a reproducible system for culturing uniform sized spheroids, because cells are relatively more adherent to a polymeric fibrous structure than PEG hydrogel, which exhibits cell-repellent characteristics and extreme hydrophilicity. These features result in spheroid formation, as they

confine cellular proliferation to the microwells. Moreover, as described in our previous study, the size of SGSC spheroids can be controlled by selecting microwells with an appropriate size.<sup>41</sup> The average size of SGSC spheroids in this study was approximately 157  $\mu\text{m}$  in 200  $\mu\text{m}$ -sized microwells; thus, we could obtain uniformly sized spheroids that were individually located in each microwell.

As the spheroids formed in the microwells were in physical contact with polymeric fibers, they could be easily affected by the properties of the polymers used in the electrospinning procedure. In the proposed system, cells could adhere to the fibrous region of the scaffolds at a certain culture temperature (37°C) and proliferate to form a full spheroid. However, lowering the culture temperature alters the polymeric property from hydrophobic to hydrophilic, which is more repellent to cellular attachment. Hence, fully formed spheroids could be successfully retrieved. The significant viability and uniform size of spheroids were effectively maintained even after complete detachment. In addition, the blending of pNIPAAm with PCL caused a slight decrease in fiber diameters, possibly because of conditional modifications in electrospinning parameters, such as a higher voltage (13 kV) for spinning than that used for bare PCL fibers (7.5 kV).

Epithelial stem cells represent adult tissue stem cells in most epithelial-cell-lined organs, and multipotent epithelial stem cells are considered to have the potential for organogenesis in adult salivary glands. Nevertheless, salivary epithelial stem cells, which participate in tissue regeneration in adult salivary tissues, are not well defined because of a lack of specific markers that distinguish stem cells from other salivary mesenchymal stromal cells or salivary progenitors, as well as a relatively slow turnover rate in the normal homeostasis process in salivary glands. During salivary gland development, the major salivary glands (parotid, submandibular, and sublingual) are derived from the ectoderm.<sup>42</sup> Recently, numerous studies have demonstrated that salivary epithelial progenitors express various putative markers, including cytokeratin 5 (KRT5), cytokeratin 14 (KRT14), Achaete-Scute family BHKH transcription factor 3 (ASCL3), SOX2, or KIT, as specific progenitor populations that contribute to salivary morphogenesis or homeostasis.<sup>43–49</sup> Recently, we observed that LGR5-expressing adult SGSCs are likely to be present in the outermost of the epithelium or the interstitium of the salivary glands, to exhibit salivary resident epitheliomesenchymal stem cell features, and to replenish salivary acinar and ductal cells upon irradiation damages.<sup>25</sup> Stem cell-related genes (*LGR4*, *LGR5*, *LGR6*, *NANOG*, and *SOX2*) were upregulated when they were cultured in thermoresponsive microwells in this study, suggesting that stem cell functions could be primed under 3D spheroid culture.

In this study, we implanted 3D SGSC<sup>spheroid</sup> cells into irradiated mouse SMGs at 2 weeks post-irradiation and observed engraftment, salivary gland function, and micro- and

micromorphology for 16 weeks after irradiation. Although more SGSCs were engrafted in SGSC<sup>spheroid</sup>-implanted SMGs than in SGSC<sup>monolayer</sup>-implanted SMGs at 2 weeks after implantation, a small number (~10 cells per field, X40) of GFP-expressing SGSCs was found to be viable in the recipient SMGs. This result implies that the therapeutic effects of SGSCs may be attributed to paracrine effects, by which SGSCs could protect cells from radiation-induced cell death and promote tissue regeneration. Indeed, in our experiment, 3D SGSC<sup>spheroid</sup> expressed more paracrine factor-related genes (*EGF*, *IGF-1*, *FGF1*, *FGF2*, and *HGF*) than 2D SGSC<sup>monolayer</sup> cells. In our previous studies, we demonstrated that growth factors, including EGF, FGFs, and HGF, could exhibit cell protective effects against radiation-induced salivary cell death.<sup>50–52</sup> IGF-1 is known to participate in DNA repair and enrich salivary gland stem and/or progenitor cells.<sup>53,54</sup> Furthermore, salivary gland ECM is known to incorporate and release these growth factors to maintain the SGSC homeostasis microenvironment.<sup>55</sup> Although the key factors involved in anti-apoptotic radioprotection and tissue remodeling after irradiation must be identified, we observed that SGSC<sup>spheroid</sup> cell-implanted mice experienced lower levels of radiation-induced tissue damage through enhanced radioprotective effects, compared with SGSC<sup>monolayer</sup> cell-implanted mice during observational study for 16 weeks post-irradiation.

In our experiments, the salivary glands of mice after irradiation did not show macroscopic recovery, and transplanted SGSCs only elicited alleviation effects on radiation-damaged salivary glands. We employed a subacute radiation damage model, by which mice were irradiated with fractionated X-ray radiation at a dose of 7.5 Gy/day for 3 days and were given treatment 2 weeks after radiation. Although an irradiation-induced mice model is still a useful model because it is easy to implant into the capsule of salivary glands just beneath the neck skin and it allows researchers to investigate the effects of radioprotectants and regeneration remedies, it might not completely recapitulate human tissue reactions. Furthermore, xenograft of human stem cells into mice may also be considered although stem cells show immune evasion and immune modulating properties. To gain further insights into human disease and the mechanisms of therapeutic candidates, other ex vivo or in vitro models, such as irradiation damage organoid models, could be used in the future.<sup>50,56</sup>

We observed that AQP5<sup>+</sup> pro-acinar cells in the SGSC<sup>spheroid</sup> group exhibited a less DNA damage and cell death and higher proliferative activity than those in the SGSC<sup>monolayer</sup> group. However, we were unable to determine whether SGSC<sup>spheroid</sup> cells outperformed SGSC<sup>monolayer</sup> cells in the preservation of MIST1<sup>+</sup> mature acinar cells, mucin-production, and saliva production at 16 weeks after irradiation. These findings suggest that we need to continue to optimize our protocol. Stem cell or spheroid delivery carriers that enable the maintenance of stem cell

characteristics of 3D spheroids or enhance the engraftment in transplanted tissues could be another way to overcome these limitations. Many preclinical studies have been tried for a decade to restore the function of salivary glands by transplanting stem cells. Unfortunately, however, few clinical trials are in progress because of hurdles to clinical trials. For translation of preclinical findings, more efforts should be made to achieve proof of concepts, verify modes of action, validate clinical efficacy, assuage safety concerns, and optimize the protocols of disease models, cell engineering techniques, transplantation dose, timing, and delivery routes.

## Conclusions

This study demonstrated that a combination of electrospinning and hydrogel patterning processes could produce thermoresponsive fiber-based microwells that could enable the retrieval of spheroids of a uniform size at temperatures below the LCST. After the retrieval of SGSC spheroids, we observed that their stem cell functions were enhanced, particularly the upregulation of paracrine-related genes. Hence, the delivery of SGSC<sup>spheroid</sup> cells provided increased opportunities for the regeneration of damaged tissues and restoration of their deteriorated functions at 16 weeks post-irradiation. The radioprotection of pro-acinar cells by the inhibition of cell death and promotion of proliferative activity resulted in the preservation of epithelial cell compartments in irradiated SMGs and in the restoration of secretory function. Thus, thermoresponsive fiber-based microwells may act as a good platform for the culture of SGSCs that can be implanted into irradiated salivary glands and provide protection against radiation therapy.

## Author contributions

Hye Jin and Jae-Min contributed equally to this manuscript. They performed the experiments, data analysis, and wrote the manuscript. Won-Gun and Jae-Yol designed and directed the project. Soohyun, DoJin, and Yeo-Jun performed animal studies, subsequent analysis, and interpreted data. Hwajung prepared fibrous scaffolds. All authors discussed the results and contributed to the final manuscript.

## Declaration of conflicting interests

The author(s) declared no potential conflicts of interest with respect to the research, authorship, and/or publication of this article.

## Funding

The author(s) disclosed receipt of the following financial support for the research, authorship, and/or publication of this article: This work was supported by the Basic Science Research Program, through the National Research Foundation of Korea (NRF), funded by the Ministry of Science, ICT, and Future Planning (NRF-2018R1A2B3004269 and NRF-2020M3A9I4039045, Republic of Korea) and ICONS (Institute of Convergence Science), Yonsei University.

## Ethical statement

Human salivary gland samples were obtained from non-tumor-bearing surgical specimens of head and neck cancer patients after obtaining informed consent from patients and approval from the Institutional Review Board of Inha University Hospital (permission number #2015–10–001). All animal experiments were approved by the Institutional Animal Care and Use Committee at Yonsei University College of Medicine and conformed to Avison Biomedical Research Center guidelines (Approval number: 2017-0092).

## ORCID iD

Jae-Yol Lim  <https://orcid.org/0000-0002-9757-6414>

## Supplemental material

Supplemental material for this article is available online.

## References

- Jensen DH, Oliveri RS, Trojahn Kølbe SF, et al. Mesenchymal stem cell therapy for salivary gland dysfunction and xerostomia: a systematic review of preclinical studies. *Oral Surg Oral Med Oral Pathol Oral Radiol* 2014; 117: 335–342.e1.
- Karp JM and Leng Teo GS. Mesenchymal stem cell homing: the devil is in the details. *Cell Stem Cell* 2009; 4: 206–216.
- Foster AA, Marquardt LM and Heilshorn SC. The diverse roles of hydrogel mechanics in injectable stem cell transplantation. *Curr Opin Chem Eng* 2017; 15: 15–23.
- Kim SJ, Kim EM, Yamamoto M, et al. Engineering multicellular spheroids for tissue engineering and regenerative medicine. *Adv Healthc Mater* 2020; 2020: e2000608.
- Xu Y, Shi T, Xu A, et al. 3D spheroid culture enhances survival and therapeutic capacities of MSCs injected into ischemic kidney. *J Cell Mol Med* 2016; 20: 1203–1213.
- Cho RJ, Kim YS, Kim JY, et al. Human adipose-derived mesenchymal stem cell spheroids improve recovery in a mouse model of elastase-induced emphysema. *BMB Rep* 2017; 50: 79–84.
- Kim M, Yun HW, Park DY, et al. Three-dimensional spheroid culture increases exosome secretion from mesenchymal stem cells. *Tissue Eng Regen Med* 2018; 15: 427–436.
- Kim JH and Lee JY. Multi-spheroid-loaded human acellular dermal matrix carrier preserves its spheroid shape and improves in vivo adipose-derived stem cell delivery and engraftment. *Tissue Eng Regen Med* 2020; 17: 565–566.
- Lv D, Hu Z, Lu L, et al. Three-dimensional cell culture: A powerful tool in tumor research and drug discovery. *Oncol Lett* 2017; 14: 6999–7010.
- Lin RZ and Chang HY. Recent advances in three-dimensional multicellular spheroid culture for biomedical research. *Biotechnol J* 2008; 3: 1172–1184.
- Sakai Y and Nakazawa K. Technique for the control of spheroid diameter using microfabricated chips. *Acta Biomater* 2007; 3: 1033–1040.
- Li Z, Guo X, Sun L, et al. A simple microsphere-based mold to rapidly fabricate microwell arrays for multisize 3D tumor culture. *Biotechnol Bioeng* 2020; 117: 1092–1100.
- Liu D, Chen S and Win Naing M. A review of manufacturing capabilities of cell spheroid generation technologies

- and future development. *Biotechnol Bioeng* 2021; 118: 542–554.
14. Agarwal S, Wendorff JH and Greiner A. Use of electrospinning technique for biomedical applications. *Polymer* 2008; 49: 5603–5621.
  15. Lee HJ and Koh WG. Hydrogel micropattern-incorporated fibrous scaffolds capable of sequential growth factor delivery for enhanced osteogenesis of hMSCs. *ACS Appl Mater Interfaces* 2014; 6: 9338–9348.
  16. Lee HJ, Kim HS, Kim HO, et al. Micropatterns of double-layered nanofiber scaffolds with dual functions of cell patterning and metabolite detection. *Lab Chip* 2011; 11: 2849–2857.
  17. Chua KN, Lim WS, Zhang P, et al. Stable immobilization of rat hepatocyte spheroids on galactosylated nanofiber scaffold. *Biomaterials* 2005; 26: 2537–2547.
  18. Lee HW, Kook Y-M, Lee HJ, et al. A three-dimensional co-culture of HepG2 spheroids and fibroblasts using double-layered fibrous scaffolds incorporated with hydrogel micropatterns. *RSC Adv* 2014; 4: 61005–61011.
  19. Shin HS, Lee S, Hong HJ, et al. Stem cell properties of human clonal salivary gland stem cells are enhanced by three-dimensional priming culture in nanofibrous microwells. *Stem Cell Res Ther* 2018; 9: 74.
  20. Cooperstein MA and Canavan HE. Biological cell detachment from poly(N-isopropyl acrylamide) and its applications. *Langmuir* 2010; 26: 7695–7707.
  21. Nakajima K, Honda S, Nakamura Y, et al. Intact microglia are cultured and non-invasively harvested without pathological activation using a novel cultured cell recovery method. *Biomaterials* 2001; 22: 1213–1223.
  22. Tang Z and Okano T. Recent development of temperature-responsive surfaces and their application for cell sheet engineering. *Regen Biomater* 2014; 1(1): 91–102.
  23. Yang J, Yamato M, Kohno C, et al. Cell sheet engineering: recreating tissues without biodegradable scaffolds. *Biomaterials* 2005; 26: 6415–6422.
  24. Chen M, Dong M, Havelund R, et al. Thermo-responsive Core–Sheath electrospun nanofibers from poly(N-isopropylacrylamide)/polycaprolactone blends. *Chem Mater* 2010; 22: 4214–4221.
  25. Yi T, Lee S, Choi N, et al. Single cell clones purified from human parotid glands display features of multipotent epitheliomesenchymal stem cells. *Sci Rep* 2016; 6: 36303.
  26. Cho JM, Yun SM, Choi YH, et al. Xanthohumol prevents dextran sulfate sodium-induced colitis via inhibition of IKK $\beta$ /NF- $\kappa$ B signaling in mice. *Oncotarget* 2018; 9: 866–880.
  27. Rockwood DN, Chase DB, Akins RE, et al. Characterization of electrospun poly(N-isopropyl acrylamide) fibers. *Polymer* 2008; 49: 4025–4032.
  28. Gu SY, Wang Z-M, Li JB, et al. Switchable wettability of thermo-responsive biocompatible nanofibrous films created by electrospinning. *Macromol Mater Eng* 2010; 295: 32–36.
  29. Foraida ZI, Kamaldinov T, Nelson DA, et al. Elastin-PLGA hybrid electrospun nanofiber scaffolds for salivary epithelial cell self-organization and polarization. *Acta Biomater* 2017; 62: 116–127.
  30. Chan YH, Huang TW, Chou YS, et al. Formation of post-confluence structure in human parotid gland acinar cells on PLGA through regulation of E-cadherin. *Biomaterials* 2012; 33: 464–472.
  31. Chou YS, Young TH and Lou PJ. Effects of biomaterial-derived fibroblast conditioned medium on the  $\alpha$ -amylase expression of parotid gland acinar cells. *Acta Biomater* 2015; 27: 214–223.
  32. Shubin AD, Felong TJ, Schutrum BE, et al. Encapsulation of primary salivary gland cells in enzymatically degradable poly(ethylene glycol) hydrogels promotes acinar cell characteristics. *Acta Biomater* 2017; 50: 437–449.
  33. Lee HW, Hsiao YC, Young TH, et al. Maintenance of the spheroid organization and properties of glandular progenitor cells by fabricated chitosan based biomaterials. *Biomater Sci* 2018; 6: 1445–1456.
  34. Nam K, Jones JP, Lei P, et al. Laminin-111 peptides conjugated to fibrin hydrogels promote formation of lumen containing parotid gland cell clusters. *Biomacromolecules* 2016; 17: 2293–2301.
  35. Nam K, Wang CS, Maruyama CLM, et al. L1 peptide-conjugated fibrin hydrogels promote salivary gland regeneration. *J Dent Res* 2017; 96: 798–806.
  36. Ozdemir T, Fowler EW, Liu S, et al. Tuning hydrogel properties to promote the assembly of salivary gland spheroids in 3D. *ACS Biomater Sci Eng* 2016; 2: 2217–2230.
  37. Srinivasan PP, Patel VN, Liu S, et al. Primary salivary human stem/progenitor cells undergo microenvironment-driven acinar-like differentiation in hyaluronate hydrogel culture. *Stem Cells Transl Med* 2017; 6: 110–120.
  38. Maria OM, Liu Y, El-Hakim M, et al. The role of human fibronectin- or placenta basement membrane extract-based gels in favouring the formation of polarized salivary acinar-like structures. *J Tissue Eng Regen Med* 2017; 11: 2643–2657.
  39. Bécavin T, Kuchler-Bopp S, Kökten T, et al. Well-organized spheroids as a new platform to examine cell interaction and behaviour during organ development. *Cell Tissue Res* 2016; 366: 601–615.
  40. Soscia DA, Sequeira SJ, Schramm RA, et al. Salivary gland cell differentiation and organization on micropatterned PLGA nanofiber craters. *Biomaterials* 2013; 34: 6773–6784.
  41. Shin HS, Kook YM, Hong HJ, et al. Functional spheroid organization of human salivary gland cells cultured on hydrogel-micropatterned nanofibrous microwells. *Acta Biomater* 2016; 45: 121–132.
  42. Rothova M, Thompson H, Lickert H, et al. Lineage tracing of the endoderm during oral development. *Dev Dyn* 2012; 241: 1183–1191.
  43. Kwon HR and Larsen M. The contribution of specific cell subpopulations to submandibular salivary gland branching morphogenesis. *Curr Opin Genet Dev* 2015; 32: 47–54.
  44. Zhang H, Boddupally K, Kandyba E, et al. Defining the localization and molecular characteristic of minor salivary gland label-retaining cells. *Stem Cells* 2014; 32: 2267–2277.
  45. Kwak M, Alston N and Ghazizadeh S. Identification of stem cells in the secretory complex of salivary glands. *J Dent Res* 2016; 95: 776–783.
  46. Chibly AM, Querin L, Harris Z, et al. Label-retaining cells in the adult murine salivary glands possess characteristics of adult progenitor cells. *PLoS One* 2014; 9: e107893.
  47. Bullard T, Koek L, Roztocil E, et al. Ascl3 expression marks a progenitor population of both acinar and ductal cells in mouse salivary glands. *Dev Biol* 2008; 320: 72–78.



48. Nelson DA, Manhardt C, Kamath V, et al. Quantitative single cell analysis of cell population dynamics during submandibular salivary gland development and differentiation. *Biol Open* 2013; 2: 439–447.
49. Emmerson E, May AJ, Berthoin L, et al. Salivary glands regenerate after radiation injury through SOX2-mediated secretory cell replacement. *EMBO Mol Med* 2018; 10(3): e8051. DOI: 10.15252/emmm.201708051
50. Cho JM, Yoon YJ, Lee S, et al. Retroductal delivery of epidermal growth factor protects salivary progenitors after irradiation. *J Dent Res* 2021; 100: 883–890.
51. Yoon YJ, Shin HS and Lim JY. A hepatocyte growth factor/MET-induced antiapoptotic pathway protects against radiation-induced salivary gland dysfunction. *Radiother Oncol* 2019; 138: 9–16.
52. Shin HS, Lee S, Kim YM, et al. Hypoxia-activated adipose mesenchymal stem cells prevents irradiation-induced salivary hypofunction by enhanced paracrine effect through fibroblast growth factor 10. *Stem Cells* 2018; 36: 1020–1032.
53. Grundmann O, Fillinger JL, Victory KR, et al. Restoration of radiation therapy-induced salivary gland dysfunction in mice by post therapy IGF-1 administration. *BMC Cancer* 2010; 10: 417.
54. Meyer S, Chibly AM, Burd R, et al. Insulin-like growth Factor-1-Mediated DNA repair in irradiated salivary glands is sirtuin-1 dependent. *J Dent Res* 2017; 96: 225–232.
55. Zhang S, Sui Y, Fu X, et al. Specific complexes derived from extracellular matrix facilitate generation of structural and drug-responsive human salivary gland microtissues through maintenance stem cell homeostasis. *J Tissue Eng Regen Med* 2020; 14: 284–294.
56. Pringle S, Maimets M, van der Zwaag M, et al. Human salivary gland stem cells functionally restore radiation damaged salivary glands. *Stem Cells* 2016; 34: 640–652.